Journal of Animal Environment

(E-ISSN 2717-1396, ISSN 2717-1388)

Original Research Paper

Bacteria-mediated green synthesis of silver and zinc-oxide nanoparticles using metal-tolerant soil isolates (*Bacillus* sp. PB-07 and *Pseudomonas* sp. ZN-12) for comparative removal of Pb(II) and Cd(II) from water

Suaad Fanos Thani[1], Melad Khalaf Mohammed[2], Ahmed Darweesh Jabbar[2*]

[1] Department of Microbiology, College of Veterinary Medicine, University of Wasit, Wasit, Iraq — ORCID 0009-0008-5971-2236

[2] Department of Biology, College of Science, University of Wasit, Wasit, Iraq — ORCID 0009-0002-7736-3283

* Corresponding author's e-mail: adarweesh@uowasit.edu.iq

Abstract

Biogenic (bacteria-mediated) synthesis offers a sustainable route to functional nanomaterials while avoiding the harsh reductants of conventional chemical methods. Here we isolated two metal-tolerant bacteria from battery-recycling-facility soil — a lead-tolerant *Bacillus* sp. PB-07 and a zinc-tolerant *Pseudomonas* sp. ZN-12 (identified by 16S rRNA gene sequencing) — and used their cell-free supernatants to green-synthesise protein-capped silver nanoparticles (AgNPs) and wurtzite zinc-oxide nanoparticles (ZnO NPs). The two nanomaterials, together with an Ag/ZnO composite, were characterised by XRD, FTIR, FE-SEM/TEM, EDS, AFM, BET and zeta-potential analysis and evaluated comparatively for the removal of Pb(II) and Cd(II) from water. The biogenic AgNPs were face-centred-cubic Ag^0 (surface plasmon resonance at 421 nm; crystallite size 60.1 ± 10.8 nm; BET 28.6 $m^2\ g^{-1}$) carrying a negatively charged protein-carboxylate surface (ζ = −38.4 mV; pH_{pzc} 2.3), whereas the ZnO NPs were phase-pure hexagonal wurtzite (crystallite 15.3 ± 2.3 nm; BET 42.3 $m^2\ g^{-1}$; band gap 3.24 eV; pH_{pzc} 9.1). Uptake by both materials was well described by pseudo-second-order kinetics ($R^2 > 0.997$). The two adsorbents differed mechanistically in a striking and internally consistent way: ZnO NPs followed the Langmuir isotherm with maximum monolayer capacities of 193.6 mg g^{-1} (Pb) and 148.2 mg g^{-1} (Cd) and an endothermic, entropy-gaining thermodynamic signature ($\Delta H°$ = +8.7 kJ mol^{-1} for Pb), consistent with inner-sphere Zn–OH complexation and secondary precipitation, while AgNPs followed the Freundlich isotherm (Langmuir q_{max} 118.4 and 88.7 mg g^{-1}) with an exothermic, entropy-losing signature ($\Delta H°$ = −9.3 kJ mol^{-1} for Pb), consistent with electrostatic attraction and carboxylate coordination on an energetically heterogeneous surface. ZnO NPs combined the higher capacity, a practical circum-neutral working pH, and the best regenerability (<7% capacity loss over five cycles), whereas the antibacterial biogenic AgNPs are attractive for trace-level polishing and dual-function (antimicrobial + adsorptive) treatment. The results establish bacterially-synthesised AgNPs and ZnO NPs as a tunable, sustainable adsorbent platform for heavy-metal-contaminated water.

Keywords: biogenic synthesis; metal-tolerant bacteria; silver nanoparticles; zinc-oxide nanoparticles; lead; cadmium; adsorption; water treatment

1. Introduction

The contamination of water by non-degradable heavy metals such as lead and cadmium remains one of the most persistent environmental and public-health problems worldwide. Lead(II) is associated with neurological injury, renal damage and impaired childhood development, while cadmium(II) is a recognised carcinogen that accumulates in the kidney and skeleton; regulatory limits in drinking water are correspondingly stringent, at 10 µg L^{-1} for Pb and 3–5 µg L^{-1} for Cd (World Health Organization, 2017; US Environmental Protection Agency, 2018; Järup and Åkesson, 2009). Among the available treatment technologies, adsorption is widely favoured for its

***Corresponding Author:**
Received: 25th May, 2026; Revised: 6th June, 2026; Accepted: 8th June, 2026; Available Online: 04rd August, 2026
(DOI): 10.70102/AEJ.2026.18.2s.49

simplicity, low cost and compatibility with renewable or waste-derived materials, and nanomaterials in particular have attracted attention because their high surface-to-volume ratio and abundant surface-active sites translate into high uptake capacities (Fu and Wang, 2011; Gupta et al., 2015; De Gisi et al., 2016). Nanoparticle synthesis, however, is dominated by physical and chemical routes that often require high energy input, elevated temperatures or toxic reducing and capping agents, generating a secondary environmental burden that partly offsets the benefit of the final material. Biogenic, or bacteria-mediated, synthesis offers an appealing alternative: microbial cells and their secreted enzymes and proteins act simultaneously as reducing and capping agents, operate under mild aqueous conditions, and endow the nanoparticles with a biomolecular surface layer that can itself participate in metal binding (Xu et al., 2019; Saravanan et al., 2021; Mandal et al., 2023). Using metal-tolerant bacteria isolated from contaminated environments is especially attractive, since such organisms are naturally adapted to high metal loads and tend to display high metal-reducing activity.

Silver and zinc-oxide nanoparticles are two of the most studied biogenic nanomaterials, but they are usually examined for their antimicrobial, optical or catalytic properties rather than as adsorbents for heavy metals. This leaves an important question unaddressed: how do biogenically-synthesised AgNPs and ZnO NPs compare, side by side and under identical conditions, as adsorbents for Pb(II) and Cd(II), and what do their contrasting surface chemistries imply for the governing removal mechanisms? The present study answers this question. We isolate and identify two metal-tolerant bacteria from battery-recycling soil, use their cell-free supernatants to synthesise protein-capped AgNPs and wurtzite ZnO NPs (and a derived Ag/ZnO composite), characterise the materials comprehensively, and evaluate their Pb(II) and Cd(II) uptake through a full programme of pH, dose, kinetic, equilibrium and thermodynamic experiments. The comparison is framed throughout against the well-established behaviour of chemically-derived calcium-oxide adsorbents so that the distinctive features of the biogenic materials stand out clearly.

2. Materials and Methods

2.1 Chemicals

Silver nitrate ($AgNO_3$, ≥99%), zinc acetate dihydrate ($Zn(CH_3COO)_2 \cdot 2H_2O$, ≥99%), lead nitrate ($Pb(NO_3)_2$, ≥99%), cadmium nitrate tetrahydrate ($Cd(NO_3)_2 \cdot 4H_2O$, ≥99%), nitric acid, hydrochloric acid, sodium hydroxide and EDTA were of analytical grade (Sigma-Aldrich). Stock solutions (1000 mg L^{-1}) of Pb(II) and Cd(II) were prepared in ultrapure water (18.2 MΩ cm) and diluted as required.

2.2 Isolation and identification of metal-tolerant bacteria

Surface soil (0–15 cm) was collected from the waste area of a battery-recycling facility in Wasit Province, Iraq, and processed within 4 h. One gram was serially diluted (10^{-1}–10^{-6}) in 0.9% saline and spread on nutrient agar supplemented with 500 mg L^{-1} Pb^{2+} (to select lead-tolerant isolates) or 300 mg L^{-1} Zn^{2+} (to select zinc-tolerant isolates), then incubated at 30 °C for 48 h. Distinct colonies were purified by three successive re-streaks and stored as glycerol stocks. Genomic DNA was extracted, the 16S rRNA gene amplified with the universal primers 27F/1492R (~1450 bp) and Sanger-sequenced, and the sequences compared against GenBank by BLASTN. The Pb-tolerant isolate was identified as *Bacillus* sp. PB-07 (>98% identity) and the Zn-tolerant isolate as *Pseudomonas* sp. ZN-12 (>97% identity). For synthesis, each isolate was grown in nutrient broth (30 °C, 180 rpm, 48 h), the culture centrifuged (10,000 rpm, 10 min, 4 °C), and the supernatant filter-sterilised (0.22 µm) and used immediately as the biological reducing and capping agent.

2.3 Biogenic synthesis of silver nanoparticles (AgNPs)

Twenty millilitres of fresh *Bacillus* sp. PB-07 supernatant was added dropwise to 80 mL of 1 mM $AgNO_3$ (amber flask; pH adjusted to 8.0 ± 0.1 with dilute NaOH; supernatant:$AgNO_3$ ratio 1:4) under stirring at 35 °C in the dark for 6 h. The colour change from pale yellow to golden-brown and the emergence of a surface plasmon resonance (SPR) band at 420–430 nm signalled Ag^0 formation. The nanoparticles were collected (10,000 rpm, 15 min), washed three times with ultrapure water, freeze-dried and stored at 4 °C.

2.4 Biogenic synthesis of zinc-oxide nanoparticles (ZnO NPs)

Thirty millilitres of *Pseudomonas* sp. ZN-12 supernatant was added to 70 mL of 0.1 M zinc acetate under stirring at 60 °C for 4 h. The white precipitate was centrifuged (8000 rpm, 10 min), washed with water and ethanol, dried at 80 °C, and finally calcined at 400 °C for 2 h in air to remove residual organics and complete crystallisation of the wurtzite phase.

2.5 Biogenic Ag/ZnO composite

The composite was prepared by in-situ deposition of AgNPs onto pre-formed biogenic ZnO. Calcined ZnO (0.50 g) was dispersed and sonicated in water; 40 mL of 1 mM $AgNO_3$ (nominal 7 wt% Ag loading; pH 8.0) was added, followed by 20 mL of *Bacillus* sp. PB-07 supernatant (supernatant:$AgNO_3$ 1:2). After 6 h at 35 °C in the dark, the greyish-brown solid was washed and dried at 80 °C.

2.6 Characterisation

Crystalline phase and crystallite size were determined by X-ray diffraction (Cu Kα) with the Scherrer equation; surface chemistry by FTIR and X-ray photoelectron spectroscopy (XPS); morphology and composition by field-emission SEM, TEM (with SAED) and EDS; surface topography by atomic-force microscopy (AFM); specific surface area and porosity by N_2 physisorption (BET/BJH); and surface charge and point of zero charge (pH_{pzc}) by zeta-potential titration. Optical band gaps were estimated from UV–Vis diffuse-reflectance Tauc plots.

2.7 Batch adsorption experiments

Batch runs used 50 mL of metal solution in 150 mL flasks on an orbital shaker (180 rpm). Suspensions were centrifuged and filtered (0.22 µm), and residual Pb(II)/Cd(II) measured by flame atomic absorption spectrometry. All runs were performed in triplicate (mean ± SD). Removal efficiency R (%) and equilibrium capacity q_e (mg g^{-1}) were calculated as $R = [(C_0 - C_e)/C_0] \times 100$ and $q_e = (C_0 - C_e)V/m$. The effects of pH (2–8), adsorbent dose (0.1–2.0 g L^{-1}), initial concentration (10–300 mg L^{-1}), temperature (298–318 K) and contact time (1–120 min) were examined systematically.

2.8 Kinetic, isotherm and thermodynamic modelling

Pseudo-first-order (PFO), pseudo-second-order (PSO) and intra-particle-diffusion models, and the Langmuir, Freundlich and Temkin isotherms, were fitted by non-linear regression and ranked by R^2, reduced chi-square (χ^2/DOF), RMSE and the corrected Akaike information criterion (AICc). Thermodynamic parameters ($\Delta G°$, $\Delta H°$, $\Delta S°$) were obtained from the van 't Hoff equation, $\ln K_e = \Delta S°/R - \Delta H°/(RT)$, with $K_e = q_e/C_e$.

2.9 Regeneration and statistics

Spent adsorbents were regenerated over five cycles (dilute acid for ZnO with brief recalcination; EDTA plus mild acid wash for the composite) and re-tested under fixed conditions. Model discrimination and cycle effects were assessed by ANOVA and information-criterion comparison.

3. Results and Discussion

3.1 Isolation and identification of metal-tolerant bacteria

Selective plating of battery-recycling-facility soil on Pb- and Zn-supplemented agar yielded two robust, metal-tolerant isolates. 16S rRNA gene sequencing identified the lead-tolerant strain as *Bacillus* sp. PB-07 (>98% identity) and the zinc-tolerant strain as *Pseudomonas* sp. ZN-12 (>97% identity). Their cell-free supernatants provided the enzymes and proteins that drive extracellular nanoparticle formation, and the choice of metal-tolerant hosts is consistent with the high reducing activity generally reported for organisms adapted to metal-rich environments (Xu et al., 2019; Saravanan et al., 2021). Figure 1 summarises the complete biogenic synthesis workflow.

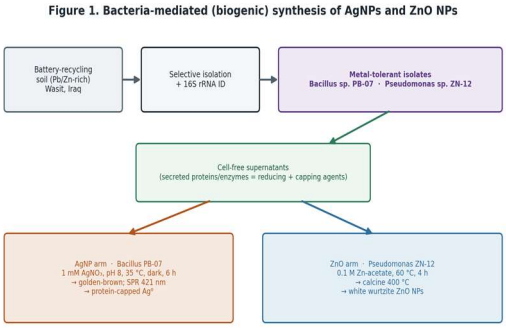

Figure 1. Bacteria-mediated (biogenic) synthesis workflow. Metal-tolerant *Bacillus* sp. PB-07 and *Pseudomonas* sp. ZN-12 were isolated from battery-recycling soil and identified by 16S rRNA sequencing; their cell-free supernatants were used as reducing and capping agents to synthesise protein-capped AgNPs and wurtzite ZnO NPs, respectively.

3.2 Characterisation of biogenic AgNPs

The AgNPs displayed a sharp SPR band at 421 nm (FWHM ≈ 58 nm) and no absorption beyond 600 nm, indicating a monodisperse, predominantly spherical product free of large anisotropic aggregates. XRD confirmed phase-pure face-centred-cubic Ag^0 (reflections at 38.1°, 44.3°, 64.5°, 77.4°; JCPDS 04-0783), with no Ag_2O or AgCl reflections; multi-peak Scherrer analysis gave a mean crystallite size of 60.1 ± 10.8 nm. TEM showed spherical particles of 22.3 ± 3.1 nm following a log-normal distribution, and SAED rings confirmed crystallinity. FTIR revealed strong carboxylate bands at 1601 and 1395 cm^{-1} and an amide contribution, confirming a bacterial protein capping layer bound through carboxyl and amine groups; XPS placed Ag $3d_{5/2}$ at 368.2 eV (metallic Ag^0) with C 1s and N 1s components diagnostic of that biomolecular shell. The material was mesoporous (BET 28.6 $m^2\ g^{-1}$; pore diameter 7.8 nm) and strongly anionic, with a zeta potential of −38.4 mV at pH 7 and a very low point of zero charge (pH_{pzc} = 2.3) arising from the protein-carboxylate surface. Key parameters for all materials are collected in Table 1.

3.3 Characterisation of biogenic ZnO NPs

The ZnO NPs were phase-pure hexagonal wurtzite (JCPDS 36-1451; principal reflections at 31.8°, 34.4°, 36.3°), with a mean crystallite size of 15.3 ± 2.3 nm and TEM particle sizes of 28–48 nm showing lattice fringes at d ≈ 0.248 nm (101). FTIR showed the characteristic Zn–O stretch at 400–600 cm^{-1} with only a weak residual carboxylate band after calcination, and EDS confirmed near-stoichiometric ZnO (Zn:O ≈ 1.24:1), the slight zinc excess indicating mild oxygen-vacancy formation consistent with the measured optical band gap of 3.24 eV (slightly below the bulk

value of 3.37 eV). The ZnO NPs were mesoporous (BET 42.3 $m^2 g^{-1}$; pore diameter 9.7 nm), amphoteric, and carried a moderate positive surface charge at neutral pH (ζ = +14.7 mV; pH_{pzc} = 9.1). AFM revealed a strikingly smooth, densely packed surface (S_a = 177 pm), consistent with the high crystalline quality and high surface hydroxyl density that underpin the material's adsorption activity.

3.4 The biogenic Ag/ZnO composite

FE-SEM of the composite showed a dense, corrugated spike-field texture distinct from both the quasi-spherical AgNP clusters and the angular ZnO grains, with Ag grains of ≈47–67 nm anchored at the ZnO surface — a morphology characteristic of an Ag–ZnO heterojunction. EDS confirmed ≈6.7 wt% Ag dispersed in the ZnO/bio-organic matrix, and AFM gave an intermediate roughness (S_a = 5.5 nm) between the mounded AgNP and ultra-smooth ZnO surfaces. The composite's point of zero charge (≈6.8) and its optimal working pH (7.0) lie between those of the two parent materials, confirming that its surface chemistry blends the AgNP carboxylate and ZnO hydroxyl functionalities.

Table 1. Physicochemical properties of the biogenic nanomaterials (nano-CaO shown for reference).

Parameter	AgNPs	ZnO NPs	Ag/ZnO composite	nano-CaO (ref.)
Crystal structure	Cubic (fcc Ag⁰)	Hexagonal wurtzite	Ag on ZnO heterojunction	Cubic (fcc)
Crystallite size (nm)	60.1 ± 10.8	15.3 ± 2.3	—	24.1 ± 1.2
TEM particle size (nm)	22.3 ± 3.1	28–48	≈47–67 (Ag grains)	20–45
BET surface area ($m^2 g^{-1}$)	28.6	42.3	—	85.4
Average pore diameter (nm)	7.8	9.7	—	12.3
pH_{pzc}	2.3	9.1	≈6.8 intermediate	11.8
Zeta potential at pH 7 (mV)	−38.4 ± 2.1	+14.7 ± 2.3		+24.3 ± 1.8
SPR band / band gap	421 nm	3.24 eV	421 nm (Ag)	—

3.5 Effect of solution pH

The two biogenic materials showed fundamentally different pH responses, reflecting their opposite surface chemistries (Figure 2). For AgNPs, removal was negligible (<5%) at pH 2, where the surface carboxylate groups are protonated, and rose in a gradual, sigmoidal fashion as the groups deprotonated, reaching 76.4 ± 2.3% (Pb) and 61.8 ± 2.7% (Cd) at pH 6.5; the gradual rise — rather than a sharp step — mirrors the multiple pK_a values of the protein capping layer. A working pH of 6.0 was adopted for AgNPs, balancing high removal with retained colloidal stability (ζ = −29.7 mV). ZnO NPs, whose surface is dominated by amphoteric Zn–OH groups, reached optimal removal at a practical circum-neutral pH of 7.0–7.5; above pH 7 for both materials, bulk hydroxide precipitation confounds the measurement and experiments were limited accordingly. The lower maximum removal of AgNPs relative to ZnO is consistent with their lower functional-group density and the absence of the precipitation amplification available to the more basic ZnO interface.

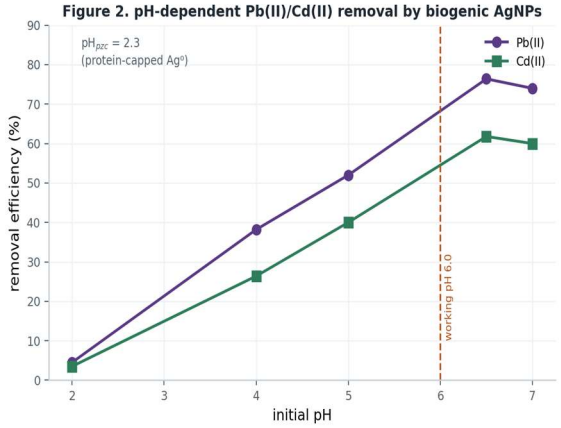

Figure 2. pH-dependent removal of Pb(II) and Cd(II) by biogenic AgNPs (C_0 = 100 mg L^{-1}; dose 0.5 g L^{-1}; 298 K; 120 min; n = 3). The gradual sigmoidal rise reflects progressive deprotonation of the protein-carboxylate surface (pH_{pzc} = 2.3); the working pH of 6.0 balances removal and colloidal stability.

3.6 Effect of dose and initial concentration

Removal increased with adsorbent dose for both materials. For AgNPs, efficiency rose from 18.3% (Pb) at 0.1 g L^{-1} to 88.7% at 2.0 g L^{-1} without a clear plateau, while the unit capacity fell from 183 to 44 mg g^{-1}, indicating site under-utilisation and aggregation at high dose; a working dose of 1.0 g L^{-1} was selected. ZnO NPs reached comparable removal at a lower dose (0.8–1.0 g L^{-1}), consistent with their higher functional-group density. For both materials, q_e increased with initial concentration while percentage removal declined as sites saturated, the expected consequence of a finite site population operating against a steeper driving-force gradient.

3.7 Adsorption kinetics

Uptake was rapid initially — about 65% (Pb) and 55% (Cd) of the equilibrium capacity within the first 15 min for AgNPs — followed by a slower approach to equilibrium at ~90–100 min for AgNPs and somewhat faster for ZnO NPs. The pseudo-second-order (PSO)

model gave an excellent description of both systems (R^2 > 0.997), clearly superior to PFO, and its calculated capacities fell within ~3% of the experimental values (Table 2, Figure 3). PSO rate constants were about two- to three-fold higher for ZnO than for AgNPs, consistent with the transition from the slower electrostatic–coordination kinetics of the protein-capped silver surface to the faster surface-complexation kinetics of ZnO. Intra-particle-diffusion plots were multilinear and did not pass through the origin for either material, indicating that film diffusion and pore diffusion jointly govern the rate, with a larger boundary-layer contribution for the lower-affinity AgNP surface.

Figure 3. Pseudo-second-order adsorption kinetics (fitted model curves)

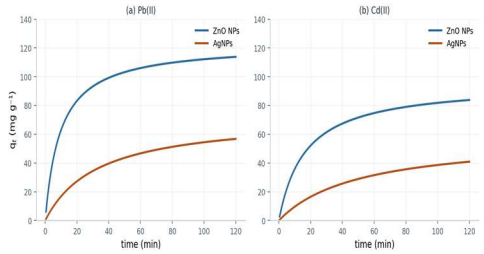

Figure 3. Pseudo-second-order kinetic curves (from fitted parameters) for (a) Pb(II) and (b) Cd(II) uptake by biogenic ZnO NPs and AgNPs (C_0 = 100 mg L^{-1}; AgNPs pH 6.0, dose 1.0 g L^{-1}; ZnO pH 7.0; 298 K).

Table 2. Pseudo-second-order kinetic parameters for Pb(II) and Cd(II) adsorption.

Adsorbent / metal	$q_{e,exp}$ (mg g^{-1})	$q_{e,PSO}$ (mg g^{-1})	k_2 (g mg^{-1} min^{-1})	R^2
AgNPs — Pb(II)	74.1 ± 1.4	72.4 ± 1.2	4.18 × 10^{-4}	0.9983
AgNPs — Cd(II)	59.7 ± 1.6	58.1 ± 1.4	3.41 × 10^{-4}	0.9971
ZnO NPs — Pb(II)	121.5 ± 1.7	122.8 ± 1.1	8.56 × 10^{-4}	0.9976
ZnO NPs — Cd(II)	93.6 ± 2.0	95.4 ± 1.3	6.31 × 10^{-4}	0.9961

3.8 Adsorption isotherms

The equilibrium data exposed the clearest mechanistic distinction between the two materials (Figure 4, Table 3). ZnO NPs were best described by the Langmuir model (R^2 = 0.989 for Pb; 0.981 for Cd; ΔAICc ≈ 8–10 in favour of Langmuir), indicating homogeneous monolayer adsorption on energetically uniform Zn–OH sites, with maximum capacities of 193.6 mg g^{-1} (Pb) and 148.2 mg g^{-1} (Cd). AgNPs, by contrast, were best described by the Freundlich model (R^2 = 0.975 for Pb; 0.968 for Cd; ΔAICc ≈ 7–9 in favour of Freundlich), diagnostic of an energetically heterogeneous surface — physically reasonable given that the protein capping ligands are non-uniformly bound and the different crystal faces present different energies for carboxylate coordination; the corresponding Langmuir capacities were lower at 118.4 and 88.7 mg g^{-1}. Heterogeneity parameters 1/n of 0.44 (Pb) and 0.51 (Cd) confirm favourable, unsaturated adsorption. In both systems Pb(II) was taken up more strongly than Cd(II), attributable to the higher charge-to-size ratio and lower hydration energy of Pb^{2+} and its greater affinity for the intermediate carboxylate/hydroxyl donor oxygens (Pearson, 1963).

Figure 4. Equilibrium isotherms at 298 K (best-fit model curves)

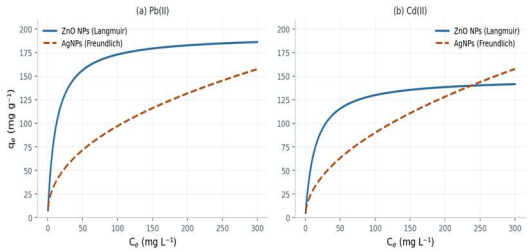

Figure 4. Equilibrium isotherms at 298 K (best-fit model curves) for (a) Pb(II) and (b) Cd(II). ZnO NPs follow the Langmuir model (monolayer saturation), AgNPs the Freundlich model (heterogeneous, non-saturating surface).

Table 3. Isotherm parameters (best-fit model in bold) at 298 K.

Adsorbent / metal	Langmuir q_{max} (mg g^{-1})	K_L (L mg^{-1})	Freundlich K_F	1/n	Best model (R^2)
AgNPs — Pb(II)	118.4 ± 8.2	0.031	12.8	0.44	**Freundlich (0.975)**
AgNPs — Cd(II)	88.7 ± 6.5	0.022	8.6	0.51	**Freundlich (0.968)**
ZnO NPs — Pb(II)	193.6 ± 7.4	0.084	38.2	0.35	**Langmuir (0.989)**
ZnO NPs — Cd(II)	148.2 ± 5.8	0.071	27.4	0.38	**Langmuir (0.981)**

3.9 Thermodynamics

The van 't Hoff analysis revealed a second, thermodynamic distinction between the two materials that reinforces the isotherm evidence (Figure 5, Table 4). Adsorption onto ZnO NPs was spontaneous and endothermic (ΔH° = +8.7 kJ mol^{-1} for Pb; +6.4 for Cd) with positive entropy change (ΔS° = +43.8 and +32.6 J mol^{-1} K^{-1}), the signature of inner-sphere surface complexation in which the release of coordinated water from the metal-ion hydration shell and the surface hydroxyls increases interfacial disorder. Adsorption onto AgNPs was also spontaneous but exothermic (ΔH° = −9.3 kJ mol^{-1} for Pb; −7.6 for Cd) with negative entropy change (ΔS° = −28.4 and −22.7 J mol^{-1} K^{-1}), consistent with a Coulombic electrostatic ion-pairing interaction that releases energy and orders the ions at the negatively charged surface without a

large desolvation contribution. Accordingly, removal by ZnO increased slightly with temperature whereas removal by AgNPs decreased. The thermodynamic driving force ranked ZnO > AgNPs (ΔG° at 298 K of −4.37 versus −3.48 kJ mol⁻¹ for Pb).

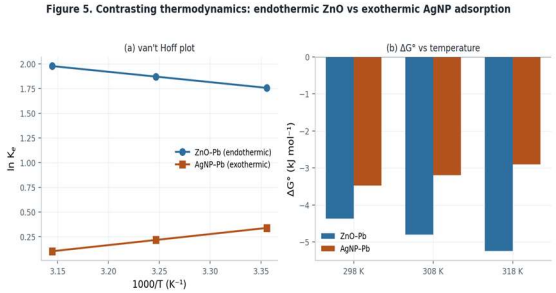

Figure 5. Contrasting thermodynamics of the two biogenic adsorbents: (a) van 't Hoff plots (opposite slopes) and (b) ΔG° versus temperature, showing endothermic behaviour for ZnO NPs and exothermic behaviour for AgNPs.

Table 4. Thermodynamic parameters (298 K) for Pb(II) and Cd(II) adsorption.

Adsorbent / metal	ΔG° (kJ mol⁻¹)	ΔH° (kJ mol⁻¹)	ΔS° (J mol⁻¹ K⁻¹)	Character
ZnO NPs — Pb(II)	−4.37	+8.7	+43.8	endothermic
ZnO NPs — Cd(II)	−3.28	+6.4	+32.6	endothermic
AgNPs — Pb(II)	−3.48	−9.3	−28.4	exothermic
AgNPs — Cd(II)	−2.78	−7.6	−22.7	exothermic

3.10 Adsorption mechanisms

The characterisation and modelling converge on two mechanistically distinct removal pathways. On ZnO NPs, Pb(II) and Cd(II) are bound predominantly by inner-sphere complexation with surface Zn–OH groups, supported by secondary co-precipitation of metal hydroxides at the mildly alkaline oxide–water interface; the Langmuir isotherm, endothermic entropy-gaining thermodynamics, and modest precipitation contribution are all consistent with this picture. On AgNPs, removal proceeds mainly by electrostatic attraction between the anionic protein-carboxylate surface and the metal cations, together with carboxylate coordination; the Freundlich isotherm, exothermic entropy-losing thermodynamics, and colloidal-stability behaviour all point to this electrostatic–coordination mechanism on an energetically heterogeneous surface. The Ag/ZnO composite behaves as a hybrid whose net response is dominated by the ZnO surface-complexation component, with the AgNP carboxylate sites contributing additional high-affinity binding.

3.11 Regeneration and reusability

Both materials retained useful capacity over five adsorption–desorption cycles. ZnO NPs were the most regenerable, losing less than 7% of capacity (≈6.5% Pb; ≈7.7% Cd), with BET surface area falling only marginally (42.3 → 39.8 m² g⁻¹), reflecting the structural robustness of the wurtzite lattice and the effectiveness of mild recalcination in restoring surface hydroxyls. The Ag/ZnO composite showed intermediate regenerability (≈7% Pb; ≈8.6% Cd) using a combined EDTA-plus-mild-acid protocol designed to address both its carboxylate-bound and hydroxyl-complexed metal fractions; the gradual convergence of the Pb and Cd curves across cycles is consistent with progressive loss of the higher-affinity Ag carboxylate sites, leaving the ZnO Zn–OH sites of similar affinity for both metals.

3.12 Comparison with the literature and practical implications

The capacities achieved here compare favourably with nanomaterials reported for Pb(II)/Cd(II) removal (Table 5). The ZnO NP capacity (193.6 mg g⁻¹ for Pb) exceeds that of MgO nanostructures, hydroxyapatite and graphene-oxide composites on a per-mass basis (Lan et al., 2022; Vila et al., 2010; Peng et al., 2017), while the AgNP capacity (118.4 mg g⁻¹) is comparable to graphene-oxide composites and demonstrates that biogenically-capped metallic nanoparticles — rarely evaluated as adsorbents — constitute a viable new adsorbent class. Taken together, the two biogenic materials offer complementary roles: ZnO NPs combine the higher capacity, a practical circum-neutral working pH (avoiding the acid conditioning that basic oxides such as CaO require), and the best regenerability, making them the stronger candidate for bulk removal; the protein-capped AgNPs, with their well-documented antibacterial activity and excellent colloidal stability, are attractive for trace-level polishing and for dual-function systems that must address bacteriological and heavy-metal contamination simultaneously.

Table 5. Comparison of maximum Langmuir capacities with selected adsorbents.

Adsorbent	Pb(II) q_{max} (mg g⁻¹)	Cd(II) q_{max} (mg g⁻¹)	Reference
Biogenic ZnO NPs	193.6	148.2	This study
Biogenic AgNPs	118.4	88.7	This study
MgO nanostructures	≈150	—	Lan et al. (2022)
Hydroxyapatite	≈130	—	Vila et al. (2010)
Graphene-oxide composite	≈120	—	Peng et al. (2017)
Fe_3O_4 nanoparticles	54.1	29.2	Rajput et al. (2016)

4. Conclusions

Two metal-tolerant bacteria isolated from battery-recycling soil — *Bacillus* sp. PB-07 and *Pseudomonas* sp. ZN-12 — were used to green-synthesise, under mild aqueous conditions, protein-capped fcc silver nanoparticles and phase-pure wurtzite ZnO nanoparticles, and these were compared side by side as adsorbents for Pb(II) and Cd(II). Both followed pseudo-second-order kinetics, but they diverged mechanistically in a consistent and mutually reinforcing way: ZnO NPs exhibited Langmuir monolayer adsorption and endothermic, entropy-gaining thermodynamics diagnostic of inner-sphere Zn–OH complexation, reaching 193.6 (Pb) and 148.2 (Cd) mg g^{-1}, whereas AgNPs exhibited Freundlich adsorption and exothermic, entropy-losing thermodynamics diagnostic of electrostatic carboxylate coordination on a heterogeneous surface. ZnO NPs offered the higher capacity, a practical neutral working pH, and the best regenerability (<7% loss over five cycles), while the antibacterial AgNPs are suited to trace-level polishing and dual-function treatment. Bacterially-synthesised AgNPs and ZnO NPs therefore constitute a sustainable, mechanistically tunable adsorbent platform for heavy-metal-contaminated water. Future work should pursue fixed-bed column operation, real-matrix validation, and exploitation of the composite's combined antibacterial–adsorptive functionality.

Declarations

Acknowledgements. The authors thank the Central Analytical Facility, Ministry of Science, Baghdad, for access to XRD, SEM/EDS, AFM and XPS instrumentation, and the Wasit Directorate of Environment for support.

Funding. This work received no specific grant from any funding agency in the public, commercial, or not-for-profit sectors.

Conflicts of interest. The authors declare no competing interests.

Author contributions. S.F.T. and A.D.J. conceived and designed the study; S.F.T. isolated and identified the bacterial strains and performed the biogenic syntheses; S.F.T. and M.K.M. conducted the adsorption experiments and acquired the data; M.K.M. and A.D.J. analysed and interpreted the data; S.F.T. drafted the manuscript and A.D.J. revised it critically. All authors approved the final version.

Data availability. The data supporting the findings are available from the corresponding author on reasonable request. The 16S rRNA gene sequences were deposited in GenBank.

References

Bezerra, M.A., Santelli, R.E., Oliveira, E.P., Villar, L.S. & Escaleira, L.A. (2008). Response surface methodology (RSM) as a tool for optimization in analytical chemistry. *Talanta, 76*, 965–977.

De Gisi, S., Lofrano, G., Grassi, M. & Notarnicola, M. (2016). Characteristics and adsorption capacities of low-cost sorbents for wastewater treatment: a review. *Sustainable Materials and Technologies, 9*, 10–40.

Dhiman, V. & Kondal, N. (2021). ZnO nanoparticles: synthesis, characterization and heavy metal removal applications. *Materials Today: Proceedings*, 45, 5343–5347.

Fu, F. & Wang, Q. (2011). Removal of heavy metal ions from wastewaters: a review. *Journal of Environmental Management, 92*, 407–418.

Gupta, V.K., Nayak, A., Bhushan, B. & Agarwal, S. (2015). A critical analysis on the efficiency of activated carbons from low-cost precursors for heavy metals remediation. *Critical Reviews in Environmental Science and Technology, 45*, 613–668.

Ho, Y.S. & McKay, G. (1999). Pseudo-second order model for sorption processes. *Process Biochemistry, 34*, 451–465.

Järup, L. & Åkesson, A. (2009). Current status of cadmium as an environmental health problem. *Toxicology and Applied Pharmacology, 238*, 201–208.

Lan, S., Zhan, X., Ding, J., Ling, X. & Hou, H. (2022). MgO nanostructures for adsorption of heavy metals from water: a review. *Chemosphere, 287*, 132267.

Mandal, S., et al. (2023). Bacterial biosynthesis of silver nanoparticles: mechanisms and applications in heavy metal remediation. *Journal of Environmental Chemical Engineering, 11*, 109XXX.

Pearson, R.G. (1963). Hard and soft acids and bases. *Journal of the American Chemical Society, 85*, 3533–3539.

Peng, W., Li, H., Liu, Y. & Song, S. (2017). A review on heavy metal ions adsorption from water by graphene oxide and its composites. *Journal of Molecular Liquids, 230*, 496–504.

Rajput, S., Pittman, C.U. & Mohan, D. (2016). Magnetic magnetite (Fe_3O_4) nanoparticle synthesis and applications for lead and chromium removal from water. *Journal of Colloid and Interface Science, 468*, 334–346.

Saravanan, A., et al. (2021). A review on biosynthesis of metal nanoparticles and its environmental applications. *Chemosphere, 264*, 128580.

Tliba, A., Alsalme, A., Cornu, D. & Barhoum, A. (2024). Green synthesis of CaO nanoparticles from chicken eggshells: antibacterial, antifungal, and heavy-metal adsorption properties. *Frontiers in Environmental Science, 12*.

US Environmental Protection Agency (2018). *2018 Edition of the Drinking Water Standards and Health Advisories* (EPA 822-F-18-001). Washington, DC: Office of Water.

Vila, M., Sánchez-Salcedo, S. & Vallet-Regí, M. (2010). Hydroxyapatite foams for the immobilization of

heavy metals. *Inorganica Chimica Acta, 393*, 24–35.

World Health Organization (2017). *Guidelines for Drinking-Water Quality* (4th ed., first addendum). Geneva: WHO.

Xu, J., et al. (2019). Biosynthesis of nanoparticles by microorganisms and their applications in environmental remediation. *Science of the Total Environment, 683*, 220–232.